Effect of cell membrane tension on the lifetime and size of mature clathrin-coated pits and their spatial distribution

Xinyue Liu, Wang Xi, Xiaobo Gong

Effect of cell membrane tension on the lifetime and size of mature clathrin-coated pits and their spatial distribution

Xinyue Liu[1,3], Wang Xi[2], Xiaobo Gong[3,4*]

[1]Shanghai Institute of Applied Mathematics and Mechanics, School of Mechanics and Engineering Science, Shanghai Key Laboratory of Mechanics in Energy Engineering, Shanghai University, Shanghai 200072, China

[2]Institut Jacques Monod, Université Paris Cité, Centre National de la Recherche Scientifique, Paris F-75013, France

[3]Key Laboratory of Hydrodynamics (Ministry of Education), Department of Engineering Mechanics, School of Naval Architecture, Ocean and Civil Engineering, Shanghai Jiao Tong University, Shanghai 200240, China

[4]Institute of Mechanobiology and Biomedical Engineering, School of Life Science and Technology, Shanghai Jiao Tong University, Shanghai 200240, China

***Correspondence:**

Xiaobo Gong

Key Laboratory of Hydrodynamics (Ministry of Education), Department of Engineering Mechanics, School of Naval Architecture, Ocean and Civil Engineering, Shanghai Jiao Tong University, Shanghai 200240, China

Email: x.gong@sjtu.edu.cn

Tel: 86-21-34207804

Abstract

Clathrin-mediated endocytosis is the most characterized pathway for cells to internalize diverse receptor-bound cargo such as proteins, nanoparticles, and viruses. However, the effect of membrane tension on clathrin-coated pit (CCP) maturation remains inadequately characterized. This study aimed to figure out the effect of membrane tension on CCP maturation spatially and temporarily, which is still a controversial and elusive issue. We obtained the sizes and spatial distributions of CCPs by the structured illumination microscopy of fixed cells and observed CCP lifetimes in live cells by total internal reflection fluorescence microscopy. The processes of CCP maturation and abortion were reproduced numerically through Monte Carlo simulation. The results showed that the growth time of CCP was more reasonably proportional to its volume rather than its surface area. We further investigated the spatial distribution of the membrane tension and size of CCPs and found a significant positive correlation between the membrane tension and the size of mature CCPs spatially, indicating that the CCPs tended to enrich in the highest-tension region, especially the mature ones. This finding agreed with our numerical prediction that the CCP structure grew larger to overcome a higher energy barrier caused by higher background cell membrane tension. Based on the aforementioned results, we speculated that when the external environment was complex, the cells might choose to reinforce the endocytic vesicles by CCPs in high-tension regions to ensure adequate nutrient uptake.

Keywords Clathrin-coated pit, CCP lifetime, CCP size distribution, mature CCP size, membrane tension

1 Introduction

Clathrin-mediated endocytosis is a widely studied process in vesicular trafficking that transports cargo molecules from the cell surface to the interior [1]. Increased membrane tension inhibits endocytosis [2] on the subcellular scale by counteracting clathrin polymerization [3] and membrane fission [4]. However, understanding the lifetime and size of clathrin-coated pits (CCPs) affected by the membrane tension remains elusive.

The CCP size and lifetime are two factors highly correlated with the productivity of CCPs. Two typical CCP catalogs were characterized through global analysis of total internal reflection fluorescence (TIRF) microscopy time series [5]: one was classified as productive that takes 30–120 s to mature, and the other was abortive with typical lifetimes (time from formation to extinction) of less than 20 s. It is believed that endocytic cargo plays a crucial role in deciding the fate of a CCP [6], and cargo binding stabilizes the CCPs and facilitates their growth toward vesicle formation. Banerjee et al. [7] developed a coarse-grained model of CCP by mapping the CCP assembly dynamics onto a one-dimensional random walk to explain the relationship between the CCP size and lifetime. Using Monte Carlo simulations, they analytically examined the statistical properties of the lifetimes and predicted the maximum size of abortive CCPs to be around 90 nm [8]. CCP structures are of various curvatures and sizes, ranging from 60 to 120 nm [9, 10], which is below the 200-nm diffraction limit of fluorescent microscopes such as TIRF or confocal microscopes. In practical terms, only cellular structures and objects at least 200 - 350 nm apart can be resolved [11]. Li et al. [12] extended the resolution of live-cell structured illumination microscopy (SIM) to 45 - 62 nm and revealed a positive correlation of 0.20 nm/s between CCP diameter and growth time by linear regression. Willy et al. [13] observed *de novo* CCPs using SIM and found that they developed a curvature in the early stages of their formation.

However, to date, the effect of cell membrane tension on the CCP size and lifetime still cannot be investigated directly.

More importantly, seminal studies conducted at the beginning of the last decade have demonstrated that cell mechanics, in particular the changes in cell membrane tension, give rise to dynamically distinct populations of clathrin-coated structures within cells [14]. It has been suggested that tension-dependent endocytosis and exocytosis are involved in surface area regulation and buffering of membrane tension. High membrane tension leads to excess exocytosis, an increase in cell surface area, and a decrease in tension, and vice versa [15]. Overall, the endocytic vesicle formation is slowed down by increased membrane tension, as high tension resists the generation of curved clathrin coats [3, 16, 17]. In a majority of these studies, the dynamics of CCSs were monitored at the plasma membrane–coverglass interface; it was found that the cell spreading area could regulate clathrin dynamics by qualitatively controlling the tension of the membrane *in vitro* [18, 19]. In practice, the local cell membrane tension on the adherent surface is difficult to be measured directly or predicted accurately with membrane–substrate interactions, confined by focal adhesions. Therefore, the observation of the bottom surface of the cell alone does not give a global picture of this problem.

In this study, the sizes and locations of CCPs were measured by the 3D scan of SIM, and the lifetimes of CCPs were acquired using TIRF. TIRF is widely used in many studies of CCPs [5, 20, 21] due to its advantages such as high temporal resolution and less laser exposure of cells that reduces the quenching of fluorescence. Thus, cells with fluorescence can be observed for a long time. The disadvantage is that TIRF can only observe the cell bottom, which is based on the total reflection principle of light. The spatial resolution of TIRF is not enough; therefore, it is insufficient to observe the size changes of CCPs during their

formation. Although the spatial resolution of SIM is considerably improved compared with that of TIRF, it is successful for individual CCP measurements [13] but difficult for high-throughput measurements of CCPs for a whole cell. SIM takes about 30 min to scan a whole cell, during which it cannot obtain a clear image due to the migration of living cells. In this situation, the cells have to be fixed during scanning by SIM; as a result, the CCP growth time cannot be obtained directly using SIM. Nevertheless, we aimed to find a way to complement the observations of SIM and TIRF. First, the growth process of CCPs observed using TIRF was reproduced by a Monte Carlo simulation, and two possible relationships between the CCP size and lifetime were examined by comparing the CCP size distribution of the Monte Carlo simulation and the experimental results. Then, the size ranges of *de novo*, developing, and mature CCPs were determined by the relationship between the CCP size and lifetime. We found the CCP size distribution was heavy-tailed compared with the standard normal distribution. In this study, we aimed to explain whether it was caused by membrane tension distribution. Further investigation of the spatial distribution of membrane tension and CCP size revealed a significant positive correlation between the membrane tension and the CCP size spatially, indicating that the CCPs tended to enrich in the highest-tension region, especially the mature ones.

It has been reported that endocytosis is randomly initiated and then stabilized by CCPs [21]. Our previous study [22] supported the idea that the CCPs behave as a mechanical reinforcement moiety in the wrapping region, which helps fend off external forces during endocytosis. Based on the simulation, we found that a larger CCP structure is needed to overcome a higher background membrane tension to assist the cargo uptake. Besides, the membrane tension distribution of a free-spread cell in arbitrary shape can be predicted through an algorithm proposed in our another previous study [23]. In the temporal aspect, the energy barrier caused by the increase in tension leads to a decrease in the number of *de novo*

CCPs [19] and an increase in the lifetime of larger-sized CCPs [12]. Interestingly, in the spatial aspect, the large-sized and long-lived CCPs are concentrated in the high-tension region in this study. To verify our point of view, we focused on how membrane tension affects the size of mature CCPs on the cell surface before pinch-off. Since the CCPs are mechanical reinforcing structures, we hypothesized that when the external environment is complex, the cells may choose to reinforce the endocytic vesicles in high-tension regions to ensure adequate nutrient uptake.

2 Results

2.1 CCP lifetime observation on cell bottom surface

The cells were starved before imaging using TIRF to ensure enough cargo-free transferrin receptors (TfRs) on the cell membrane. During imaging, transferrins (Tfs) labeled with red fluorescence were added to the cell cultures. Tfs randomly bound to TfRs and were caught by developing CCPs labeled with green fluorescence. This process is shown in Figure 1A. The frames were taken at 2-s intervals. The video is shown in Supporting Information. Limited by TIRF spatial resolution (>200 nm) [24], only red and green fluorescent clusters can be observed but not the fine size increment of CCPs. The trajectories of CCPs were identified with Imaris software using the same strategies as in the study of Jaqaman et al. [25]. A time window of two frames is the optimal gap closing with the frame rate of 0.5 Hz in our cases. Since both individual receptors and receptor aggregates generate diffraction-limited image features, the particle positions were detected by local maxima and then fitting Gaussian kernels in areas around these local maxima to achieve subpixel localization [26]. When Tf internalized through CCP, the red and green fluorescent trajectories overlapped timely and

spatially. Thus, CCPs could be identified during endocytosis according to the temporal and spatial coincidence of the two fluorescent signals. If at least one red trajectory is encountered during the lifetime of the green track, the CCPs are considered mature; if no red trajectory is encountered, the CCPs are considered abortive, as shown in the schematic diagram in Figure 1B. Figure 1C is taken from a frame in the fluorescence sequence scanned by TIRF (see Video in Supporting Information). Figure 1C(1) and (2) shows the green fluorescence of CCPs and the red fluorescence of Tfs, respectively; Figure 1C(3) is the overlapped image of CCPs and Tfs, and Figure 1C(4) shows the identified trajectories. The study of cargo and dynamin regulating CCP maturation by Loerke et al. [5] revealed two short-lived subpopulations corresponding to aborted intermediates and one longer-lived productive subpopulation. They also figured out that the longer-lived subpopulation was designated the productive population because 1) its kinetics matched those of surface-bound transferrin internalization and 2) manual tracking of 450 CCPs could be performed, yielding a similar average lifetime. Our study focused more on productive CCPs; therefore, we did not subdivide the abortive groups. In our study, 800 trajectories of the productive CCPs and 1012 trajectories of the abortive ones were identified. The CCPs already existing in the first frame or still existing in the last frame were excluded from the collective trajectories due to incomplete lifetime observation. Figure 1D and 1E shows the examples of typical trajectories of the productive and abortive groups, respectively. The CCPs and the Tfs with which they interact were coincident in time and space [Fig. 1D(1)], and they both exhibited Brownian-like motion, which was also mentioned in the study of Ehrlich et al. [21]. Figure 1D(23) shows the mean square distance (MSD) and diffusion coefficient of CCPs and Tfs. MSD refers to the average value of the square of the distance that particles or molecules move during a certain period. It can be expressed mathematically as MSD = $\langle (r(t) - r(0))^2 \rangle$. Here, $r(t)$ is the position of the particle at time t, $r(0)$ is the position of the particle at time 0, and $\langle \rangle$

represents the average value over all time-steps of particles. The relationship between the diffusion coefficient D_f and the mean square displacement MSD can be described by the Einstein relation, which, in two dimensions, can be expressed as MSD = $4D_f t$. Figure 1F (1) shows the spatial distribution of CCP number and lifetime. The lifetime has an exponential distribution, and hence the spot color is concentrated in the low lifetime region if using a linear colormap. Thus, the colormap is represented by six quantiles of CCP lifetime to better illustrate the relationship between lifetime and number of CCPs. Figure 1F (2)(3) reveals that the counts of CCPs and their lifetimes were negatively correlated (linear coefficient = –0.152, P = 0.009), which was consistent with the findings of Willy et al. [27] revealing the shortening of lifetimes with increased initiation and dissolution rates when the cells spread.

Figure 2A shows the generation intensity of CCPs in each new frame. The histogram of the CCP generation intensity is presented in Figure 2B. The Kolmogorov–Smirnov (K–S) test was conducted to test whether the CCP generation intensity satisfied the Poisson, Rayleigh, or normal distributions at the 1% significance level. The results showed that the Poisson and Rayleigh distributions failed to pass the K–S test, and the fitting were not fine either; the normal distributions could pass the K–S test. The returned value of H_0 = 1 indicated that the K–S test rejected the null hypothesis at the P < 1% significance level (Table 1). The probability density function (PDF) of CCP generation expressed by the normal distribution is $f\left(x \mid \mu_c, \sigma_c^2\right) = \frac{1}{\sqrt{2\pi\sigma_c^2}} e^{-\frac{(x-\mu_c)^2}{2\sigma_c^2}}$, and the parameter values obtained by the maximum likelihood estimates are μ_c = 13.16 ± 0.80 and σ_c = 4.78 ± 0.66 (number of all new CCPs).

Figure 2C shows the discrete and fitted cumulative distribution function (CDF) for a visual comparison of the Poisson, Rayleigh, and normal distributions, which also confirms that the normal distribution is the best. As a result, the normal distribution was used to conduct a

Monte Carlo simulation for CCP generation. Figure 2D shows the PDF of the new CCPs in each new frame. The exponential distribution $f\left(x \mid \lambda\right) = \lambda e^{-\lambda x}$ was used to estimate the expectation of CCPs' lifetimes. The lifetime expectation of the productive and abortive CCPs was λ_p^{-1} = 41.37 ± 3.03 s and λ_a^{-1} = 18.22 ± 1.18 s by maximum likelihood estimates, respectively. The longest lifetime of the productive and abortive CCPs was 250 s and 100 s in our observation, respectively, reflecting wide individual differences in CCP lifetime. It was difficult to identify whether a single CCP belonged to the productive or abortive group directly, Loerke et al. [5] solved this problem by piecewise fitting the joint PDF of the CCP lifetimes to assort the CCPs into three groups: productive, early abortive, and late abortive CCPs. The abortive group was divided into early abort (5.2 ± 0.1 s) and late abort (15.9 ± 1 s). The lifetime of the productive CCPs was 86.9 ± 5.8 s, which was best approximated by an exponentially decaying distribution. The cell line used in their study was monkey kidney epithelial cells (BSC1), whereas RBL-2H3 cells were used in our study. This might be the reason why the average lifetime of each CCP in our study was slightly different from the aforementioned results. Besides, Yang et al. [28] classified CCPs into CCPs exhibiting clathrin waves and those without clathrin waves. They reported that the lifetime of CCPs that exhibited clathrin waves (median: 37.4 ± 11.1 s; mean:32 ± 42 s) was consistently shorter than that of CCPs without clathrin waves (median: 72.5 ± 18.3 s; mean: 48 ± 38 s) in RBL-2H3 cells.

2.2 CCP size and distribution on the cell membrane

A total of 12 cells were scanned using SIM. Figure 3A shows the reconstructed fluorescence image of Cell ID. 09. The horizontal (*XY*-axis) and the vertical (*Z*-axis) scanning accuracies were 24 nm and 120 nm, respectively. The structured light reconstruction images were obtained using Nikon imaging software with a resolution of about 50 nm [29, 30]. The sizes

and positions of CCPs were identified using Imaris software, and the CCPs on the cell surface were extracted using the self-written MATLAB code. The 3D numerical reconstruction of the cell structure was performed using the built-in library function of MATLAB for convex or concave hull boundary searching based on the positions of CCPs. The geometric parameters, including cell volume, cell area, and spread area, are listed in Table S1 (Supporting Information). Heuser et al. [9] observed using the cryo-electron microscope that the size range of CCPs was 60–120 nm. It must be pointed out that the CCP size observed using the scanning electron microscope is close to its real size, while the size observed using a fluorescence microscope is much larger, because the principle of a fluorescence microscope is to illuminate fluorescent protein molecules with a laser. For example, in the SIM observation of Li et al. [12], the CCPs were large and stable enough to be resolved as a ring, which finally grew to a median maximum diameter of ~ 152 nm. Therefore, the CCP size mentioned in this study was regarded as SIM observation size. In addition, the resolutions of the Z direction and the XY plane were different for a Gaussian laser beam. Therefore, the obtained CCP diameters were the equivalent diameters. Although stochastic optical reconstruction microscopy [31] has a better spatial resolution compared with SIM, it is not high-throughput enough in temporal resolution for whole-cell scanning. SIM is a trade-off between temporal and spatial resolutions. Nevertheless, the results of SIM are still countable and reasonable for CCP size variation analysis.

Figure 3B shows the side view of the positions and sizes of CCPs. The CCP sizes were divided into seven ranges, represented by seven different colors. The CCP sizes represented by each color in all figures in the following text are consistent with those in this figure. The CCP positions and sizes on the bottom surface are randomly distributed as observed by the naked eye (Figure 3C); interestingly, the CCPs are rarely observed at the center of the cell top (Figure 3BD). Consistently, Grossier et al. [32] found that the endocytosis of Tf occurred

mostly near the bottom of the cell, with almost no endocytosis on the top surface of the cell. Meanwhile, some epidermal growth factor endocytosis occurred on the bottom surface of the cell, and it was evenly distributed on the surface of the middle part of the cell, but rarely occurred at the top of the cell. These findings could partially explain the hole of CCPs on the top of cells observed in our experiment. We also scanned over the cell top (box height 15 μm is higher than 11 μm of cell height) to ensure that this was not caused by incomplete 3D scanning; in some cases, we scanned from top to bottom to exclude the effect of fluorescence quenching. The mechanical and biological mechanisms for this phenomenon need to be further examined, which are also one of the research focuses of this study. Figure 3EF shows the scatters of the CCP number and density (number per area) within different size ranges of the 12 cells at the bottom and on the dorsal surface, respectively. Li et al. [12] found that the average CCP density was $2.83/\mu m^2$. In our research, we determined an average density of $1.54/\mu m^2$ and $1.02/\mu m^2$ at the bottom and on the dorsal surface of the total 12 cells, respectively. Although CCPs on the dorsal surface are more than those on the bottom surface, the CCPs on the bottom surface are denser than those on the dorsal surface, reflecting that endocytosis is more active on the bottom surface than on the dorsal surface. Interestingly, the CCP size and density distribution are heavy-tailed compared with the standard normal distribution. A reasonable hypothesis is that the heavy-tailed effect is probably caused by cell membrane tension distribution, which we will discuss in section 3. The method of Gaussian kernel fitting to identify particles in the TIRF image [26] is also used here to compensate for the spatial resolution.

2.3 Relationship between the CCP size and lifetime

We reproduced the growth process of CCPs by Monte Carlo simulation with their PDFs summarized via experimental data (Algorithm 1). The proportion of the abortive CCPs was

γ = 0.56 according to 1012 abortive CCPs/1812 all CCPs identified. The results of 10,000 times Monte Carlo simulations are expressed as mean and standard deviation, as the error bars shown in Figure 4A. The Monte Carlo simulation results are very close to the experimental results, verifying the rationality that the generation intensity of CCPs satisfies the normal distribution and the lifetime distribution of CCPs satisfies the exponential distribution. The proportions of all CCPs in each size range are shown as bar charts in Figure 4B. The average CCP size proportions are similar at the bottom and on the dorsal surface. Of course, the CCP size proportions of every single cell are slightly different (see Supporting Information). The CCPs of size within 100 - 250 nm (cyan, green, and yellow) account for 62.4%, which is the majority subpopulation of the total CCPs. The CCPs of size < 100 nm account for 12.0%, and the CCPs of size > 250 nm account for 25.6%. In the Monte Carlo simulation, we investigated two possible relationships between the CCP size and growth time (time from formation to current growing size), which were $t \propto r^2$ and $t \propto r^3$ intuitively, since CCPs are usually considered as shell structures mechanically [33] and they are fruit-like in shape. The simulated CCP proportions are represented by red and green error bars. The red error bars show that the CCP proportions decrease with the increase in CCP size, reflecting that the relationship $t \propto r^2$ is inconsistent with the experimental observation. The relationship $t \propto r^3$ represented by green error bars is well compared with the experimental observation, with a peak between 150 and 200 nm. As a result, it was reasonable to estimate that the CCP growth time was proportional to its volume. As we know, the resolution of SIM is about 40–60 nm, and a fluorescent spot composed of at least four pixels can be considered a CCP. Thus, the CCPs with a size < 100 nm are difficult to distinguish from noise spots. This systematic error can explain a large gap between the experimental data and the Monte Carlo simulation when the size is < 100 nm.

We terminated the Monte Carlo simulation at t = 600 s, which was the total observation time of the TIRF image sequence and a sufficiently long time to observe, to mimic the CCP size distribution observed by SIM when the cells were fixed. Figure 5 shows the results of numerical analysis. Figure 5A shows the histogram of the growth time of the CCPs still developing when the Monte Carlo simulation terminated. Different to Figure 1 and Figure 4 that we excluded the CCPs still existing in the last frame due to incomplete lifetime observation, here we counted as their growth time since they were still developing. It was also well compared with the proportion of CCP growth time observed by TIRF, further confirming that the scheme of Monte Carlo simulation was reliable and the relationship $t \propto r^3$ was reasonable. Figure 5B shows the fitting curve between the CCP size and growth time, where the growth times corresponding to the selected sizes are labeled on the axis and highlighted in colored dash lines. Among these, the CCP growth time with a size < 100 nm was only 4 s, indicating that the CCPs were captured soon after they were initiated, which was in line with the actual situation. Figure 5C shows the CDF of the CCP growth time by Monte Carlo simulation, revealing that the CCPs with a size < 200 nm had a corresponding growth time of > 24 s, which accounted for 60%. The proportion of CCPs with a size > 250 nm and a corresponding growth time > 76 s was less than 23%, which was also consistent with the experimental observation of 25.6% for the CCPs size > 250 nm. Figure 5D shows the CDF of the growth time of the productive and abortive CCPs; the corresponding PDF is already shown in Figure 4A(2–3). In Figure 5D, the lower abscissa is labeled with the growth time, and the upper abscissa is labeled with the corresponding CCP sizes by simulation using the relationship $t \propto r^3$. It shows that 95% of the abortive CCPs were of a growth time within 32 s, and only 0.2% of the abortive CCPs were of size > 250 nm. Loerke et al. [5] also presented a subset of long-lived, isolated CCPs, which were highly likely (99%) to represent productive events. The predicted the maximum size of abortive CCPs in our study is within

200 - 250 nm, compared to 90 nm predicted by Banerjee et al. [8] and the reason is also due to the observation size effect of fluorescent microscope as mentioned before. Therefore, when we investigated the relationship between the cell membrane tension distribution and CCP size, it was considered that this 0.2% of the abortive CCPs could be neglected and the CCPs with a size > 250 nm all belonged to the productive group. Above all, we divided the CCPs into three categories according to the relationship between the CCP size and growth time: 1) the size < 100 nm belonged to *de novo* CCPs mixed with a certain number of image noises, 2) the size within 100–250 nm belonged to the developing CCPs including partial abortive ones, and 3) the size >250 nm belonged to the mature CCPs in the productive group.

3 Discussion

3.1 Membrane tension distribution

Directly measuring the spatial distribution of membrane tension on spread cells via existing experimental methods remains a challenge. In our previous study [23], the cell spreading was assumed to be a quasi-static process, and the dynamic process of cell spreading from the suspension state was solved inversely through an algorithm that alternately executed a particle-based method and searched for the minimum deformation energy. A standard spread cell model was established by 3D reconstruction of the cell shapes, as shown in Figure 6A, whose geometry is the average of 12 scanned cells, as shown in Figure 3BCD. The cell-spread shapes were obtained until the minimum searching of the cell deformation energy function converged, and the membrane tension distribution was predicted using Hooke's law in which the membrane was discretized into triangular grids [23]. The first principle tension describes the maximum tensile force of the triangular element in mechanics. Tan et al. [19] confined the cells growing on micropatterns through fibronectin, presenting a quantitative analysis of how physical cues, specifically cell spreading area, altered the dynamics of CCPs.

Their results showed a positive correlation between the average cell membrane tension and the spread area. The cells with a larger spreading area have more short-lived CCPs but a higher CCP initiation rate. Inspired by their study, we calculated a square cell with the same bottom as the standard spread cell model and a circular cell with a double-bottomed area, as shown in Figure 6B and 6C. Qualitative and quantitative comparisons with previous experimental results in references [19, 34] validated the reliability of our numerical method in reference [23]. Our simulation results showed that the membrane tension gradient demonstrated a decreasing trend from the bottom to the top of the cell. Cells with larger bottom areas developed greater tension compared with cells with smaller bottom areas, and the cells with the same bottom area but a larger bottom perimeter also experience higher membrane tension (Figure 6B and 6C). Furthermore, this numerical method can be applied to estimate the membrane tension distribution of cells in any free-spreading shape (see Figure 6 D–6F and Supporting Information). The tension is higher where the filamentous pseudopodia grow. Several reports indicated that the plasma membrane tension mechanically resisted shape changes involving an increase in the total surface area of the cell. For example, the expansion of cellular protrusions was resisted by membrane tension during cell spreading [17, 35] and cell migration [36, 37]. Therefore, our estimates of tension distribution were consistent with these findings.

We examined the relevance of the CCP number, geometric parameters, and tension of the 12 cells, as shown in Figure 7; the corresponding values of these parameters are listed in Table S1 in Supporting Information. The parameters characterizing the quantity of CCPs included the CCP number, percentage of different size ranges, and density. The parameters characterizing the geometric properties of the cells included the area, volume, and height. The parameters characterizing cell membrane tension included the average and variance of tension, area expansion, volume increase, and number of pseudopodia. Interestingly, the

pseudopodia number was positively correlated with the average tension because the cells needed to consume more energy for each new pseudopodium they extend. The groups of parameters representing similar properties and showing the same positive or negative trends in correlation despite the differences in relevance values were “the number and the density of CCPs,” “the cell area, the cell volume, and the cell height,” “the area expansion and the volume increase of cells,” and “the average and the variance of tension.” More importantly, the CCP number was positively correlated with the geometric properties such as the cell area and volume, but negatively correlated with the membrane tension. In other words, the larger-sized cells had a higher CCP number, and the cells in a higher-tension state possessed a lower CCP number. The membrane tension was significantly negatively correlated with the total CCP number and slightly negatively correlated with the proportion of *de novo* CCPs, but slightly positively correlated with the proportion of the mature CCPs. The total CCP number decreased with the increase in membrane tension, which was consistent with the findings of Dai et al. [15], while the increase in the proportion of mature CCPs was a new finding in our study.

3.2 Relationship between the spatial distribution of CCPs and membrane tension

Cell ID.11, whose bottom surface was close to a circular shape, was selected to compare the CCP locations and the membrane tension distribution, considering its membrane tension distribution was close to the standard spreading cell model, as shown in Figure 8AB(1–3). Other cells are shown in Supporting Information. The CCP size histogram appeared with a heavy tail compared with the normal distribution [Figure 8A(4)]. The local membrane tensions were sorted in six quantiles (Figure 8B). The histogram of the membrane tension sorted by six equal divisions of the tension maximum was nonuniform and concentrated between 1/6 and 3/6 of the maximum tension [Figure 8B(4)]. The background membrane

tension where CCPs were located concentrated within a range of 0.15–0.35 mN/m [Figure 8C(1-2)]. Therefore, we sorted the CCPs by six quantiles of the membrane tension [Figure 8C(3–4)]. On the bottom surface, fewer CCPs were found in 0–1/2 quantiles of tension than in 1/2–1 quantiles of tension. On the dorsal surface, the CCPs with a size < 250 nm exhibited a relatively uniform distribution, while more CCPs with a size > 250 nm appeared at higher-tension quantiles.

We further compared the CCP number bar in six quantiles of membrane tension, as shown in Figure 8D(1–3). The CCP numbers were normalized by their maximum values at the bottom, on the dorsal surface, and on the total surface. The normalized average membrane tension in each quantile and within the triangular mesh area where CCPs are located is represented by "spots ♦" and "spots ◊," respectively. The CCPs number bars show similar increasing trend with both spots ♦ and ◊, and they are better fitted to the histogram of CCPs on the total surface [Figure 8D(3)] than that at the bottom [Figure 8D(1)] or on the dorsal surface [Figure 8D(2)]. Moreover, spots ♦ and ◊ are almost overlapped, indicating no obvious tension selectivity for the CCP locations. The other cells show similar trends as the Cell.ID 11 is presented in Supporting Information (Figure S1-11), indicating that the appearance of larger quantities of CCPs in the higher-tension region is probably a general pattern, especially a sharp increase in the CCP numbers in 5/6 to 1 quantile of tension, a proper reason for which is discussed later.

As analyzed earlier, the CCPs can be divided into *de novo*, developing, and mature categories according to the relationship between their size and growth time. Thus, we further analyzed the correlation between the CCP number and the area expansion rate, as shown in Figure 8D(4). The blue, green, and red dots represent the *de novo*, developing, and mature CCPs, respectively. The Rel and *P* value are the correlation coefficient and significance,

410 respectively. The normalized CCP number on the total surface was positively correlated with
411 the average membrane tension where the CCPs were located, regardless of the different CCP
412 categories. Although the CCPs with a size <100 nm appeared at a higher average tension on
413 the Cell.ID 11, this was not a general rule for the other cells. Also, the Rel and *P* value in the
414 blue CCP group varied significantly in different cells (see Supporting Information). This
415 could be explained by the CCPs' shorter lifetime if the cell membrane tension ws higher, as
416 observed by Tan et al. [19]. We found that shorter-life CCPs were of smaller sizes, as shown
417 in Figure 5. Besides, the low signal-to-noise ratio at the top of the cell due to light scattering,
418 and therefore the error in the data analysis, was higher in this CCP category. For a less
419 number of CCPs appearing in the lower-tension region, as shown in Figure 8C(3-4), the CCP
420 density distributions were checked to confirm whether it was because of a smaller area of this
421 tension region; if so, the density distributions should be close to the uniform distribution. No
422 specific pattern of density distributions with tension was observed in six quantiles, as shown
423 in Figure 8E(1–3), and the correlation analysis supported this [Figure 8E(4)]. The other cells
424 also had a random distribution of CCP densities and no significant statistical correlation
425 between densities and tensions (see Supporting Information).

426 An interesting phenomenon was a sharp increase in CCP numbers in 5/6 to 1 quantile of
427 tension. To confirm whether it was only for the Cell.ID 11 or a general rule, we examined the
428 correlation between the CCP number and the average tension for each cell, as shown in
429 Figure 9. Although within the 0 to 5/6 quantile of tension the CCP number did not always
430 monotonically increase, a sharp increase was observed in both the CCP number and the
431 average tension within the 5/6 to 1 quantile for all cells (Figure 9A and 9B). However, a
432 variation uneasy to detect was found in the percentage of different CCP sizes, with a slight
433 decrease in the percentage of CCPs <250 nm but a slight increase in the percentage of
434 CCPs >250 nm (Figure 9C and 9D), implying that more mature CCPs appeared in the higher-

tension region. The CCP number and the percentage of CCPs >100 nm showed significant correlations with the average tension in six quantiles for all the cells, but the densities of CCPs did not (Figure 9E and 9F).

3.3 Effect of membrane tension on CCP size

In our previous study [22], the CCP was modeled as a shell structure with bending rigidity. An optimization algorithm was proposed for minimizing the total energy of the system, which comprised the deforming nanoparticle, the receptor–ligand bonds, the cell membrane, and the CCP; hence, the profile of the system was acquired. As shown in Figure 10, the CCPs enable full wrapping of the nanoparticles at various membrane tensions represented by the pre-elongation rate I_e, which is a parameter to describe the degree of background tension. D is the size of nanoparticle, and the optimization algorithm needs a gussed initial CCPs size D_{c0} [Figure 10 A-D(1)]. The size of mature CCPs D_c is normalized by their initial size D_{c0}. Figure 10E shows that the normalized sizes of mature CCPs increased in a similar trend with the increase in I_e, no matter what their initial sizes were. When I_e > 1.2, most of the receptor–ligand bonds in the wrapping area broke because the CCP size increased. Thus, in high-tension conditions, nanoparticles have opportunities to leak out. When the cell membrane tension increased, the normalized deformation energy also increased in similar trends (Figure 10F), no matter what their initial sizes were. Therefore, the CCP mature size was dependent on the tension of the cell membrane rather than on the size of the nanoparticles.

Since more energy was needed for CCP maturation under higher membrane tension, it was easy to understand that the total CCP number decreased as the average tension increased (Figure 7). It has already been suggested that high membrane tension leads to excess

exocytosis, an increase in cell surface area, and a decrease in tension, and vice versa [38]. However, why the CCPs concentrate in the highest-tension range of each cell, especially the mature CCPs (essentially the molecular mechanism of how clathrins aggregate more in a higher-tension region), is still unclear. We speculated that when the external environment was complex and the cells were in a large deformation state, the cells might choose to reinforce the endocytic vesicles by CCPs in high-tension regions to ensure adequate nutrient uptake in macroscopic representations.

4 Conclusions

In this study, fixed RBL-2H3 cells were scanned using SIM and the size and spatial distribution of CCPs were obtained. The CCP lifetimes in living cells were observed using TIRF. The CCP generation intensity was best fitted by the normal distribution using the K-S test. The process of CCP formation, and then maturation or abortion, was reproduced numerically by Monte Carlo simulation. The reliability of our Monte Carlo simulation scheme was verified by comparing it with the experimental results. The CCP lifetimes satisfied the exponential distribution. Based on the simulation results, the CCP growth time was proportional to the volume of CCPs, and the CCPs could be divided into *de novo*, developing, and mature ones according to their sizes. The results also showed a positive correlation of the CCP number with the geometric properties, such as the cell area, but a negative correlation with the average membrane tension. This could be explained by CCP maturation being more difficult under higher cell membrane tension from a mechanical perspective. Further investigation of membrane tension and the spatial distribution of CCPs in six quantiles revealed a sharp increase of CCPs number in the region with the highest tension, and a significant positive correlation between membrane tension and the size of CCPs, particularly the mature ones. Although the underlying molecular mechanism was still

unclear, we speculated that when the external environment was complex, the cells might choose to reinforce the endocytic vesicles by CCPs in high-tension regions to ensure adequate nutrient uptake in macroscopic representations.

Materials and Methods

Fixed-cell 3D scanning using SIM

RBL-2H3 cells stably expressing clathrin light chain A tagged with green fluorescent proteins were cultured in minimum essential medium (MEM) (Invitrogen 11095-09) with 20% fetal bovine serum (FBS) (Sigma f4135-500 mL) and 50 μg/mL gentamicin (Invitrogen 15750-060). The cell culture conditions were 5% carbon dioxide, 37°C, and 95% humidity. After culturing in a normal medium for 24 h, the cells were washed three times with phosphate-buffered saline (PBS) (pH = 7.4) and fixed with 4% paraformaldehyde (pH = 7.4). SIM (n-sim; Nikon) is with objective lens CFI apoTIRF 100× oil (N.A. 1.49), 488-nm laser transmitter, and CCD camera (DU-897, Andor and Technology). Imaris software was used to identify green fluorescent spots and obtain their size and XYZ coordinates. It was considered that the fluorescent spots on the surface of the cell were the CCPs undergoing endocytosis, whose position was extracted using the self-built MATLAB code.

CCP interaction with Tf observed using TIRF

After culturing in a normal medium for 24 h, the cells were cultured in starvation solution without FBS for 4 h and then transferred to the image buffer for time series imaging to eliminate the influence of endocytosis signals from other proteins. During imaging, 20 μg/μL Tf Alexa Fluor 647 (Thermo Fisher) solution was added. Fluorescent images with two channels were taken every 2 s. Trajectories of red and green spots were identified using Imaris software. The temporal and spatial co-location analysis of the trajectories of red and

505 green fluorescence was programmed using the self-built MATLAB code.

506 **Algorithm. 1 Monte Carlo simulation of CCP generation**

1: **For loop j** = [1,2,3…10000]

2: **For loop t** = [0,2,4…600s]

3: Generate a random integer N_c satisfying the normal distribution $f\left(x \mid \mu_c, \sigma_c^2\right) = \frac{1}{\sqrt{2\pi\sigma_c^2}} e^{-\frac{(x-\mu_c)^2}{2\sigma_c^2}}$ as the number of new CCPs appeared at the step time **t**.

4: Generate a random number *K* with a uniform distribution of 0–1 for each new CCPs. If $K > \gamma$, assign this CCP into the productive, otherwise into the abortive group.

5: Generate a random number *M* with a uniform distribution of 0–1. For each productive CCP, if $M > \sum_{y=\tau+2}^{250} P_p(y) \Big/ \sum_{y=\tau}^{250} P_p(y)$, then mark this CCP at the end of its lifetime.

For each abortive CCP, if $M > \sum_{y=\tau+2}^{150} P_a(y) \Big/ \sum_{y=\tau}^{150} P_a(y)$, then mark this CCP as the end of the lifetime.

Calculate the size of each CCP based on two possible relationships: one is $t \propto r^2$, and the other is $t \propto r^3$.

6: **End For loop t**

7: Count the number, lifetime, and CCP size in each group.

8: **End For loop j**

---

507 The longest lifetime of the productive and abortive groups to truncate was set at 250 s and

150 s, respectively. The discrete form of PDF for productive CCPs was $P_p(\tau)=\lambda_p e^{-\lambda_p \tau}, \tau \in [0,250]$ and that for abortive CCPs was $P_a(\tau)=\lambda_a e^{-\lambda_a \tau}, \tau \in [0,150]$. The growth time proportional to the surface area $\frac{t_{\max}-t}{t_{\max}-t_{\min}}=\frac{r_{\max}^2-r^2}{r_{\max}^2-r_{\min}^2}$ and the volume of CCPs $\frac{t_{\max}-t}{t_{\max}-t_{\min}}=\frac{r_{\max}^3-r^3}{r_{\max}^3-r_{\min}^3}$ were investigated. Among these, appropriate truncation was taken according to the actual situation; thus, $t_{\max}$ = 250 s, $r_{\max}$ = 410 nm, $t_{\min}$ = 0 s, and $r_{\min}$ = 0 nm.

The method to predict the size of mature CCPs under membrane tension is presented in reference [22]. The method to simulate the membrane tension distribution of the spread cells is presented in reference [23].

Declarations

Ethics approval

Not applicable

Consent for publication

Not applicable

Availability of data and materials

The data presented in this study are available in article or supplementary material

Competing interests

The authors declare that they have no competing interests.

Funding

This study was supported in part by the National Natural Science Foundation of China (12072198) and the China Scholarship Council for Joint PhD program (201206230004). Wang Xi received funding from the Mechanobiology Institute seed grant, Ministry of Education's Academic Research Fund Tier 1 Grant (R-397-000-247-112).

Authors' contributions

Xinyue Liu carried out the studies, participated in collecting, analysis, interpretation of data and drafted the manuscript. Wang Xi performed the experiments and participated in manuscript correction. Xiaobo Gong participated in designing and writing (review/editing) of the manuscript. All authors read and approved the final manuscript.

Acknowledgments

RBL-2H3 cells stably expressing clathrin light chain A tagged with green fluorescent proteins were provided by Professor Min Wu's research group at the National University of Singapore. The experimental work was conducted at the Nanolab of Professor Chwee Teck Lim's research group at the National University of Singapore.

Abbreviations

CCP Clathrin-coated pit

CDF Cumulative distribution function

K-S test Kolmogorov–Smirnov test

MSD Mean square distance

PDF Probability density function

SIM Structured illumination microscopy

Tf Transferrin

TfR Transferrin receptor

TIRF Total internal reflection fluorescence microscopy

References

1. Kaksonen M, Roux A (2018) Mechanisms of clathrin-mediated endocytosis. Nature reviews Molecular cell biology 19:313-26 https://doi.org/10.1038/nrm.2017.132

2. Boulant S, Kural C, Zeeh JC, Ubelmann F, Kirchhausen T (2011) Actin dynamics counteract membrane tension during clathrin-mediated endocytosis. Nature cell biology 13:1124-31 https://doi.org/10.1038/ncb2307

3. Saleem M, Morlot S, Hohendahl A, Manzi J, Lenz M, Roux A (2015) A balance between membrane elasticity and polymerization energy sets the shape of spherical clathrin coats. Nature communications 6:6249 https://doi.org/10.1038/ncomms7249

4. Morlot S, Galli V, Klein M, Chiaruttini N, Manzi J, Humbert F et al (2012) Membrane shape at the edge of the dynamin helix sets location and duration of the fission reaction. Cell 151:619-29 https://doi.org/10.1016/j.cell.2012.09.017

5. Loerke D, Mettlen M, Yarar D, Jaqaman K, Jaqaman H, Danuser G et al (2009) Cargo and dynamin regulate clathrin-coated pit maturation. PLoS biology 7:e57 https://doi.org/10.1371/journal.pbio.1000057

6. Kirchhausen T (2009) Imaging endocytic clathrin structures in living cells. Trends in cell biology 19:596-605 https://doi.org/10.1016/j.tcb.2009.09.002

7. Banerjee A, Berezhkovskii A, Nossal R (2012) Stochastic model of clathrin-coated pit assembly. Biophysical journal 102:2725-30 https://doi.org/10.1016/j.bpj.2012.05.010

8. Banerjee A, Berezhkovskii A, Nossal R (2012) Distributions of lifetime and maximum size of abortive clathrin-coated pits. Physical review E, Statistical, nonlinear, and soft matter physics 86:031907 https://doi.org/10.1103/PhysRevE.86.031907

9. Heuser J (1980) Three-dimensional visualization of coated vesicle formation in fibroblasts. The Journal of cell biology 84:560-83 https://doi.org/10.1083/jcb.84.3.560

10. Pearse BM, Crowther RA (1987) Structure and assembly of coated vesicles. Annual review of biophysics and biophysical chemistry 16:49-68 https://doi.org/10.1146/annurev.bb.16.060187.000405

11. Schermelleh L, Heintzmann R, Leonhardt H (2010) A guide to super-resolution fluorescence microscopy. The Journal of cell biology 190:165-75 https://doi.org/10.1083/jcb.201002018

12. Li D, Shao L, Chen BC, Zhang X, Zhang M, Moses B et al (2015) ADVANCED IMAGING. Extended-resolution structured illumination imaging of endocytic and cytoskeletal dynamics. Science (New York, NY) 349:aab3500 https://doi.org/10.1126/science.aab3500

13. Willy NM, Ferguson JP, Akatay A, Huber S, Djakbarova U, Silahli S et al (2021) De novo endocytic clathrin coats develop curvature at early stages of their formation. Developmental cell 56:3146-59.e5 https://doi.org/10.1016/j.devcel.2021.10.019

14. Djakbarova U, Madraki Y, Chan ET, Kural C (2021) Dynamic interplay between cell membrane tension and clathrin-mediated endocytosis. Biology of the cell 113:344-73 https://doi.org/10.1111/boc.202000110

15. Dai J, Ting-Beall HP, Sheetz MP (1997) The secretion-coupled endocytosis correlates with membrane tension changes in RBL 2H3 cells. The Journal of general physiology 110:1-10 https://doi.org/10.1085/jgp.110.1.1

16. Ferguson JP, Willy NM, Heidotting SP, Huber SD, Webber MJ, Kural C (2016) Deciphering dynamics of clathrin-mediated endocytosis in a living organism. The Journal of cell biology 214:347-58 https://doi.org/10.1083/jcb.201604128

17. Gauthier NC, Masters TA, Sheetz MP (2012) Mechanical feedback between membrane tension and dynamics. Trends in cell biology 22:527-35 https://doi.org/10.1016/j.tcb.2012.07.005

18. Yonashiro R, Sugiura A, Miyachi M, Fukuda T, Matsushita N, Inatome R et al (2009) Mitochondrial ubiquitin ligase MITOL ubiquitinates mutant SOD1 and attenuates mutant SOD1-induced reactive oxygen species generation. Molecular biology of the cell 20:4524-30 https://doi.org/10.1091/mbc.e09-02-0112

19. Tan X, Heureaux J, Liu AP (2015) Cell spreading area regulates clathrin-coated pit dynamics on micropatterned substrate. Integrative biology : quantitative biosciences from nano to macro 7:1033-43 https://doi.org/10.1039/c5ib00111k

20. Cureton DK, Harbison CE, Cocucci E, Parrish CR, Kirchhausen T (2012) Limited transferrin receptor clustering allows rapid diffusion of canine parvovirus into clathrin endocytic structures. Journal of virology 86:5330-40 https://doi.org/10.1128/jvi.07194-11

21. Ehrlich M, Boll W, Van Oijen A, Hariharan R, Chandran K, Nibert ML et al (2004) Endocytosis by random initiation and stabilization of clathrin-coated pits. Cell 118:591-605 https://doi.org/10.1016/j.cell.2004.08.017

22. Liu X, Yang H, Liu Y, al e (2019) Numerical study of clathrin-mediated endocytosis of nanoparticles by cells under tension. Acta Mech Sin 35:691-701 https://doi.org/10.1007/s10409-019-00839-0

618 23. Liu X, Tsubota K, Yu Y, al e (2022) A numerical method to predict the tension
619 distribution on the membrane of spreading cells based on the reconstruction of focal
620 adhesions. Sci China Phys Mech Astron https://doi.org/10.1007/s11433-021-1873-1

621 24. Betzig E, Patterson GH, Sougrat R, Lindwasser OW, Olenych S, Bonifacino JS et al
622 (2006) Imaging intracellular fluorescent proteins at nanometer resolution. Science (New York,
623 NY) 313:1642-5 https://doi.org/10.1126/science.1127344

624 25. Jaqaman K, Loerke D, Mettlen M, Kuwata H, Grinstein S, Schmid SL et al (2008)
625 Robust single-particle tracking in live-cell time-lapse sequences. Nature methods 5:695-702
626 https://doi.org/10.1038/nmeth.1237

627 26. Thomann D, Rines DR, Sorger PK, Danuser G (2002) Automatic fluorescent tag
628 detection in 3D with super-resolution: application to the analysis of chromosome movement.
629 Journal of microscopy 208:49-64 https://doi.org/10.1046/j.1365-2818.2002.01066.x

630 27. Willy NM, Ferguson JP, Huber SD, Heidotting SP, Aygün E, Wurm SA et al (2017)
631 Membrane mechanics govern spatiotemporal heterogeneity of endocytic clathrin coat
632 dynamics. Molecular biology of the cell 28:3480-8 https://doi.org/10.1091/mbc.E17-05-0282

633 28. Yang Y, Xiong D, Pipathsouk A, Weiner OD, Wu M (2017) Clathrin Assembly
634 Defines the Onset and Geometry of Cortical Patterning. Developmental cell 43:507-21.e4
635 https://doi.org/10.1016/j.devcel.2017.10.028

636 29. Gustafsson MG (2005) Nonlinear structured-illumination microscopy: wide-field
637 fluorescence imaging with theoretically unlimited resolution. Proceedings of the National
638 Academy of Sciences of the United States of America 102:13081-6
639 https://doi.org/10.1073/pnas.0406877102

30. Lin PY, Ge J, Kuang C, al e (2014) Fluorescence detection and lifetime imaging with stimulated emission, in: Opt. Nanoscopy Nov Microsc Tech:161-78

31. Huang B, Wang W, Bates M, Zhuang X (2008) Three-dimensional super-resolution imaging by stochastic optical reconstruction microscopy. Science (New York, NY) 319:810-3 https://doi.org/10.1126/science.1153529

32. Grossier JP, Xouri G, Goud B, Schauer K (2014) Cell adhesion defines the topology of endocytosis and signaling. The EMBO journal 33:35-45 https://doi.org/10.1002/embj.201385284

33. Jin AJ, Prasad K, Smith PD, Lafer EM, Nossal R (2006) Measuring the elasticity of clathrin-coated vesicles via atomic force microscopy. Biophysical journal 90:3333-44 https://doi.org/10.1529/biophysj.105.068742

34. Pietuch A, Janshoff A (2013) Mechanics of spreading cells probed by atomic force microscopy. Open biology 3:130084 https://doi.org/10.1098/rsob.130084

35. Raucher D, Sheetz MP (2000) Cell spreading and lamellipodial extension rate is regulated by membrane tension. The Journal of cell biology 148:127-36 https://doi.org/10.1083/jcb.148.1.127

36. Houk AR, Jilkine A, Mejean CO, Boltyanskiy R, Dufresne ER, Angenent SB et al (2012) Membrane tension maintains cell polarity by confining signals to the leading edge during neutrophil migration. Cell 148:175-88 https://doi.org/10.1016/j.cell.2011.10.050

37. Lieber AD, Yehudai-Resheff S, Barnhart EL, Theriot JA, Keren K (2013) Membrane tension in rapidly moving cells is determined by cytoskeletal forces. Current biology : CB 23:1409-17 https://doi.org/10.1016/j.cub.2013.05.063

662 38. Dai J, Sheetz MP (1995) Regulation of endocytosis, exocytosis, and shape by
663 membrane tension. Cold Spring Harbor symposia on quantitative biology 60:567-71
664 https://doi.org/10.1101/sqb.1995.060.01.060

665

666

667 **Table 1. K–S test results of the CCP generation intensity**

	Productive CCPs	Abortive CCPs	Total CCPs
Poisson distribution	H_0 = 1, P = 6.88e-04	H_0 =1, P = 0.0026	H_0 = 1, P = 2.24e-06
Rayleigh distribution	H_0 = 1, P = 3.60e-07	H_0 =1, P = 0.0013	H_0 = 1, P = 2.16e-04
Normal distribution	H_0 = 0, P = 0.1016	H_0 = 0, P = 0.4667	H_0 = 0, P = 0.2423

668

669

Figure Legends

Figure 1. (A) Schematic diagram of CCP wrapping Tfs. (B) CCPs were classified into (1) productive and (2) abortive catalogs. (C) One frame in fluorescent image sequence obtained by TIRF. (1) CCPs. (2)Tfs. (3) Overlapping of CCPs and Tfs. (4) Spots identified by Imaris. Typical trajectories of (E) productive and (F) abortive CCPs. (1) Locations of the trajectories. (2) Mean square distance of the trajectories. (3) Histogram of diffusion coefficient. (F) (1) CCPs locations colored by their lifetime, and heatmap of CCP (2) counts and (3) mean lifetime in each meshgrid.

Figure 2. (A) Numbers of new CCPs in each new frame. (B) Histogram of new CCP numbers in each new frame; they were fitted by the Rayleigh, Poisson, and normal distributions. (C) Cumulative distribution function of the new CCPs in each new frame. (D) Probability density function distribution of the new CCPs in each new frame. (1) Productive CCPs. (2) Abortive CCPs. (3) All CCPs.

Figure 3. (A) Fluorescent image of CCPs on Cell ID.09 was chosen as a demonstration observed by SIM. The CCP locations identified (B) on the total surface (side view), (C) on the bottom surface (bottom view), and (D) on the dorsal surface (top view) in the boxes of 32 $\times$ 32 $\times$ 15 μm^3. The distributions of CCP number (E) and density (F) were sorted by size on a total of 12 scanned cells.

Figure 4. (A) Proportions of the productive and abortive CCPs and their lifetime histogram, comparing the Monte Carlo simulation with the experimental data. (B) Comparison of the CCP proportions in different size ranges between the experimental observation and the Monte Carlo simulation, considering two possible relationships between the CCP size and growth time.

Figure 5. Growth time and sizes of the developing CCPs when the Monte Carlo simulation terminated. (A) Histogram of the CCP growthtime compared with the experimental values.

(B) Relationship between the CCP size and growth time fitted by $t \propto r^3$. (C) CDF of the growth time of the total simulated CCPs fitted by $t \propto r^3$. (D) CDF of the CCP growth time of experimental data with double abscissas fitted by $t \propto r^3$.

Figure 6. Numerical simulation results of the first principal membrane tension of (A) the standard spread cell model, (B) a square-bottomed cell with the same bottom area, and (C) a circular cell with a double-bottomed area compared with the standard spread cell model. (D–F) Cell ID.01-03. Cell ID.04-12 can be seen in Supporting Information.

Figure 7. Relevance of the CCP number, cell geometry, and membrane tension.

Figure 8. Comparison of the CCP locations and the membrane tension on Cell ID.11. (A1–3) CCP locations on the surface scanned by SIM. (A4) Stacked histogram of the CCP sizes on the dorsal and bottom surfaces. (B1–3) Simulated membrane tension distribution in six quantiles. (B4) Membrane tension histogram. (C1–2) Background membrane tension distribution where CCPs are located and catalogued by their size ranges. (C3–4) CCP numbers in six quantiles of the membrane tension catalogued by their size ranges. (D1–3) Stacked histogram of the CCP sizes was sorted by six tension quantiles. Spots ♦ and ◊ represent the average of the area expansion rate in each quantile and within the local areas of the CCPs, respectively. (D4) Relevance of the CCP numbers in each quantile and the average tension where CCPs were located. (E1–3) CCP density bar in each tension quantile. (E4) Relevance of the CCP density in each quantile and the average tension where CCPs were located.

Figure 9. CCP numbers (A) and average tension (B) in six quantiles of tension. The component of the CCP size (C) and the comparison of their proportion changes (D) in six

717 quantiles of tension. The relevance of the CCP number (E) and density (F) to the average of
718 tension in six quantiles.

719 **Figure 10. Size of mature CCPs increase with cell membrane tension when wrapping**
720 **nanoparticles of different diameters.** (A) *D* = 25 nm, (B) *D* = 50 nm, (C) *D* = 75 nm, and
721 (D) D = 100 nm. (E) CCP size increased with the membrane tension. (E) Deformation energy
722 increased with the membrane tension.

723

724

Supporting Information

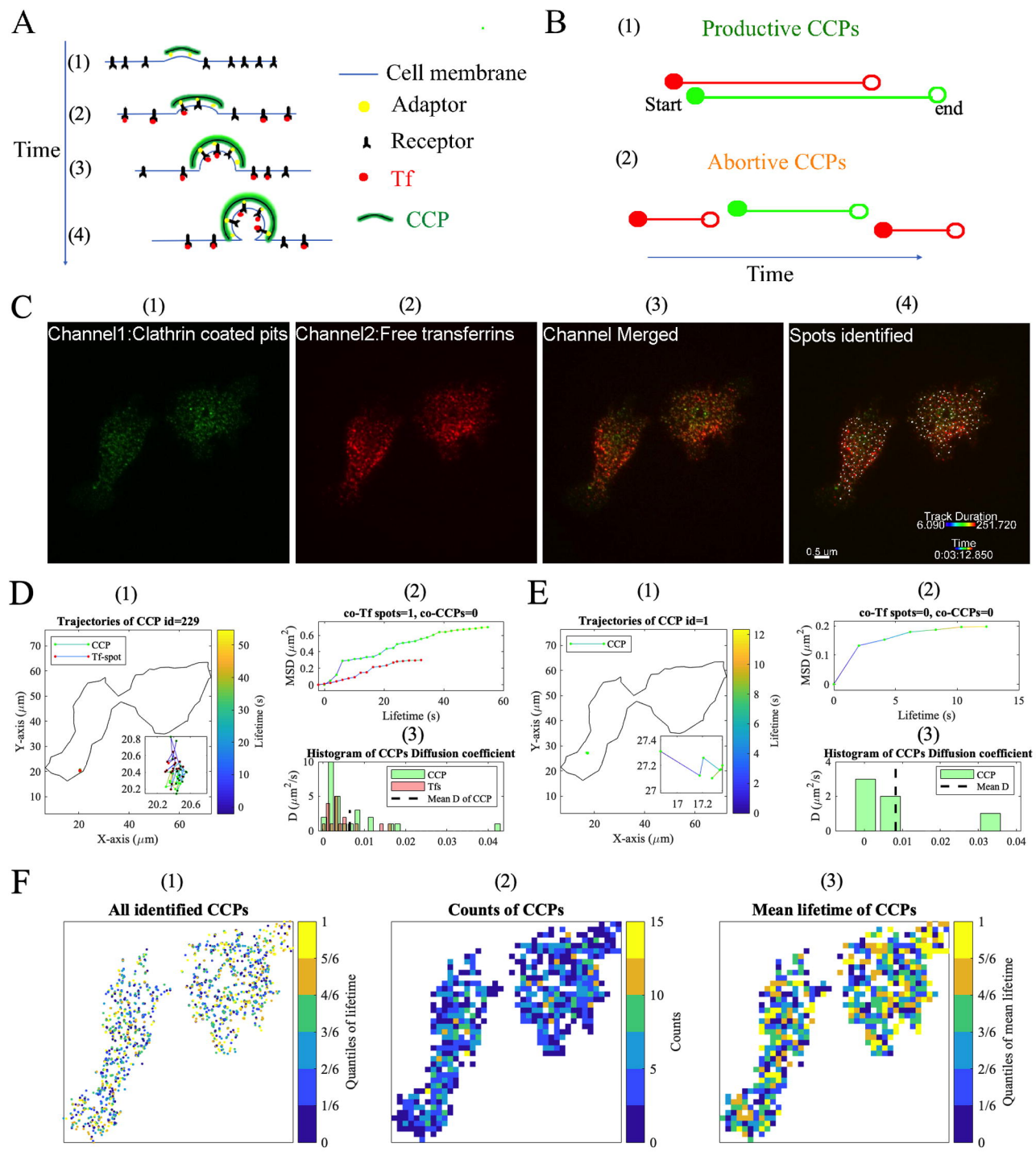
A
Time
(1)
(2)
(3)
(4)
Cell membrane
Adaptor
Receptor
Tf
CCP
B
(1)
Productive CCPs
Start
end
(2)
Abortive CCPs
Time
C
(1)
(2)
(3)
(4)
Channel1:Clathrin coated pits
Channel2:Free transferrins
Channel Merged
Spots identified
Track Duration
6.090
251.720
Time
0:03:12.850
0.5 μm
D
(1)
Trajectories of CCP id=229
CCP
Tf-spot
Y-axis (μm)
X-axis (μm)
Lifetime (s)
(2)
co-Tf spots=1, co-CCPs=0
MSD (μm²)
Lifetime (s)
(3)
Histogram of CCPs Diffusion coefficient
CCP
Tfs
Mean D of CCP
D (μm²/s)
E
(1)
Trajectories of CCP id=1
CCP
Y-axis (μm)
X-axis (μm)
Lifetime (s)
(2)
co-Tf spots=0, co-CCPs=0
MSD (μm²)
Lifetime (s)
(3)
Histogram of CCPs Diffusion coefficient
CCP
Mean D
D (μm²/s)
F
(1)
All identified CCPs
Quantiles of lifetime
(2)
Counts of CCPs
Counts
(3)
Mean lifetime of CCPs
Quantiles of mean lifetime

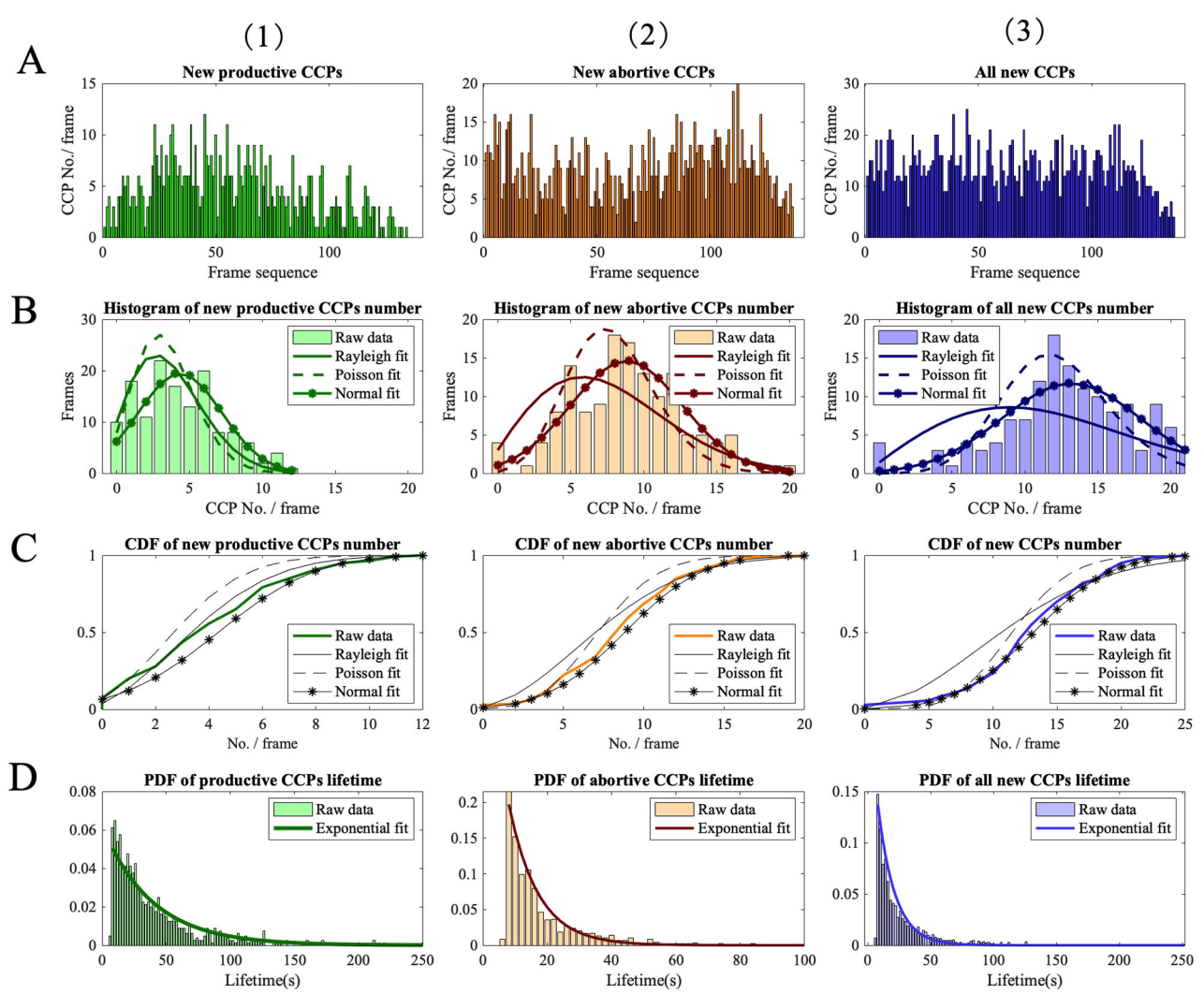
(1)
(2)
(3)
A
New productive CCPs
New abortive CCPs
All new CCPs
CCP No./ frame
Frame sequence
B
Histogram of new productive CCPs number
Histogram of new abortive CCPs number
Histogram of all new CCPs number
Frames
CCP No. / frame
Raw data
Rayleigh fit
Poisson fit
Normal fit
C
CDF of new productive CCPs number
CDF of new abortive CCPs number
CDF of new CCPs number
No. / frame
D
PDF of productive CCPs lifetime
PDF of abortive CCPs lifetime
PDF of all new CCPs lifetime
Exponential fit
Lifetime(s)

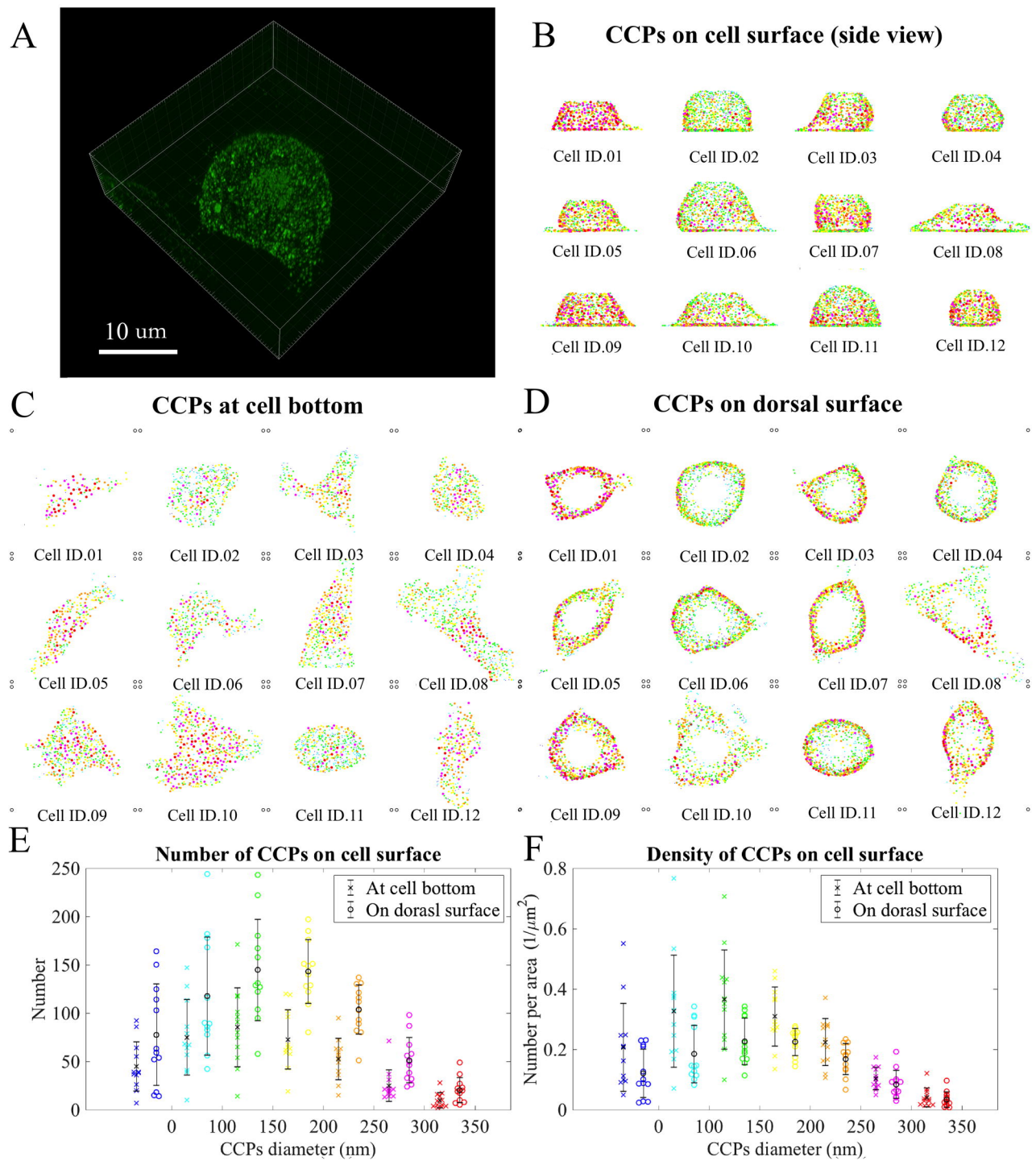
A
10 um
B
CCPs on cell surface (side view)
Cell ID.01
Cell ID.02
Cell ID.03
Cell ID.04
Cell ID.05
Cell ID.06
Cell ID.07
Cell ID.08
Cell ID.09
Cell ID.10
Cell ID.11
Cell ID.12
C
CCPs at cell bottom
D
CCPs on dorsal surface
E
Number of CCPs on cell surface
At cell bottom
On dorasl surface
Number
CCPs diameter (nm)
F
Density of CCPs on cell surface
Number per area (1/μm²)
CCPs diameter (nm)

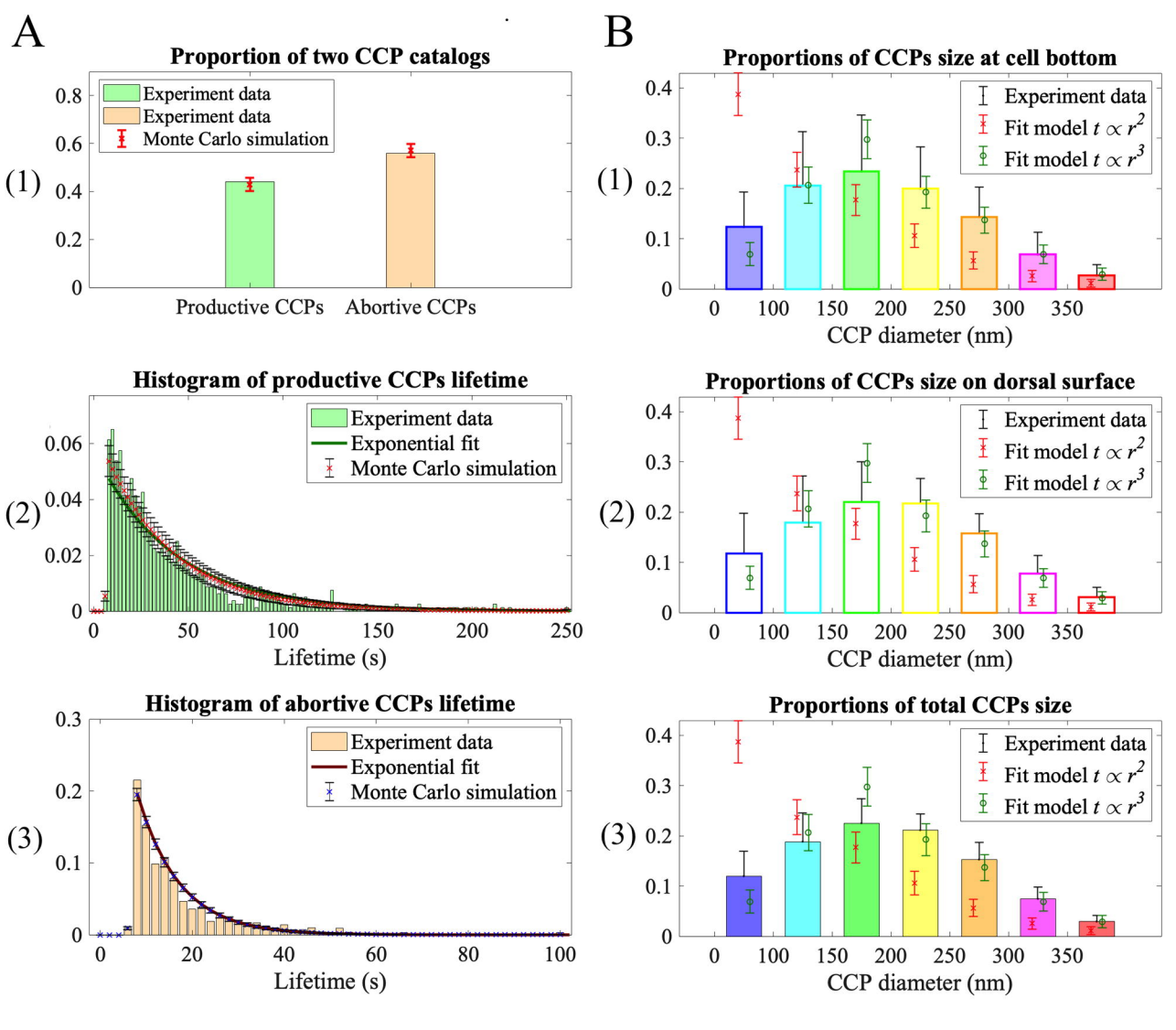
A
Proportion of two CCP catalogs
Experiment data
Experiment data
Monte Carlo simulation
(1)
0.8
0.6
0.4
0.2
0
Productive CCPs
Abortive CCPs
Histogram of productive CCPs lifetime
Experiment data
Exponential fit
Monte Carlo simulation
(2)
0.06
0.04
0.02
0
0
50
100
150
200
250
Lifetime (s)
Histogram of abortive CCPs lifetime
Experiment data
Exponential fit
Monte Carlo simulation
(3)
0.3
0.2
0.1
0
0
20
40
60
80
100
Lifetime (s)
B
Proportions of CCPs size at cell bottom
Experiment data
Fit model $t \propto r^2$
Fit model $t \propto r^3$
(1)
0.4
0.3
0.2
0.1
0
0
100
150
200
250
300
350
CCP diameter (nm)
Proportions of CCPs size on dorsal surface
Experiment data
Fit model $t \propto r^2$
Fit model $t \propto r^3$
(2)
0.4
0.3
0.2
0.1
0
0
100
150
200
250
300
350
CCP diameter (nm)
Proportions of total CCPs size
Experiment data
Fit model $t \propto r^2$
Fit model $t \propto r^3$
(3)
0.4
0.3
0.2
0.1
0
0
100
150
200
250
300
350
CCP diameter (nm)

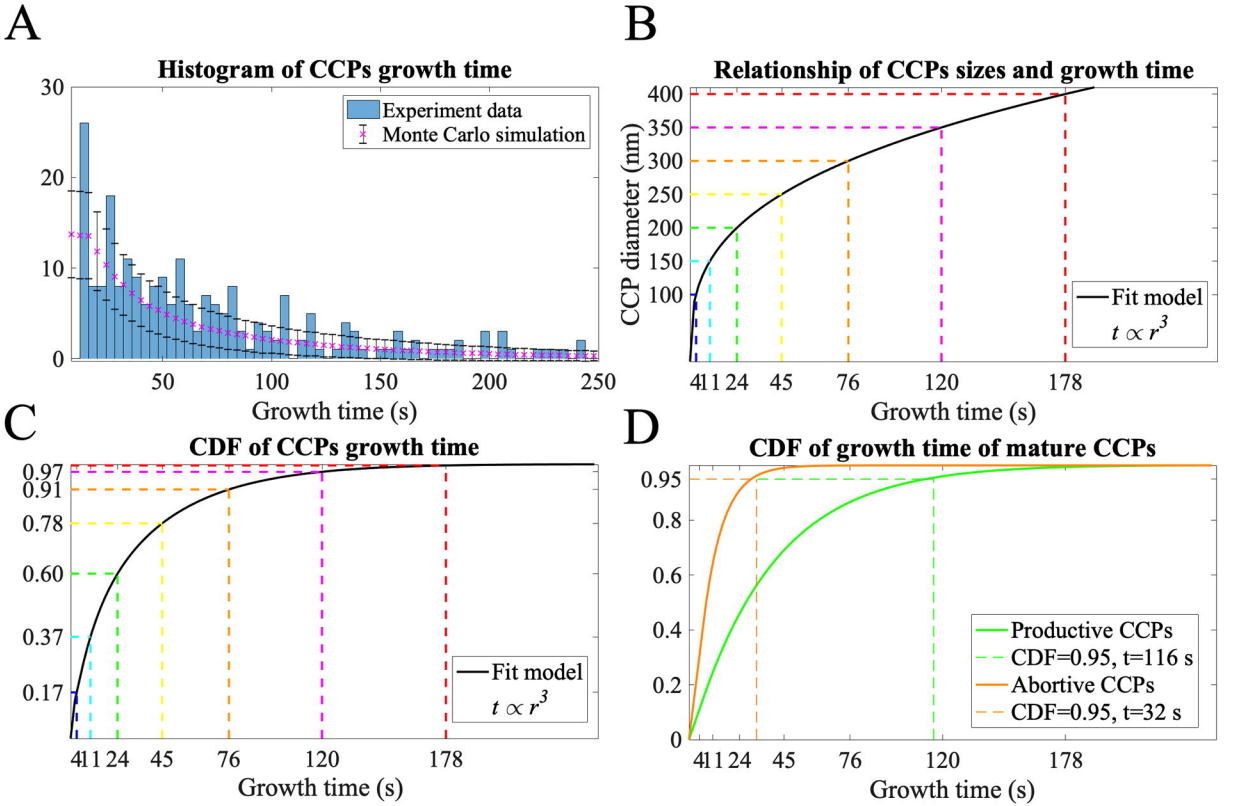
A
Histogram of CCPs growth time
Experiment data
Monte Carlo simulation
Growth time (s)
B
Relationship of CCPs sizes and growth time
CCP diameter (nm)
Fit model
$t \propto r^3$
Growth time (s)
C
CDF of CCPs growth time
Fit model
$t \propto r^3$
Growth time (s)
D
CDF of growth time of mature CCPs
Productive CCPs
CDF=0.95, t=116 s
Abortive CCPs
CDF=0.95, t=32 s
Growth time (s)

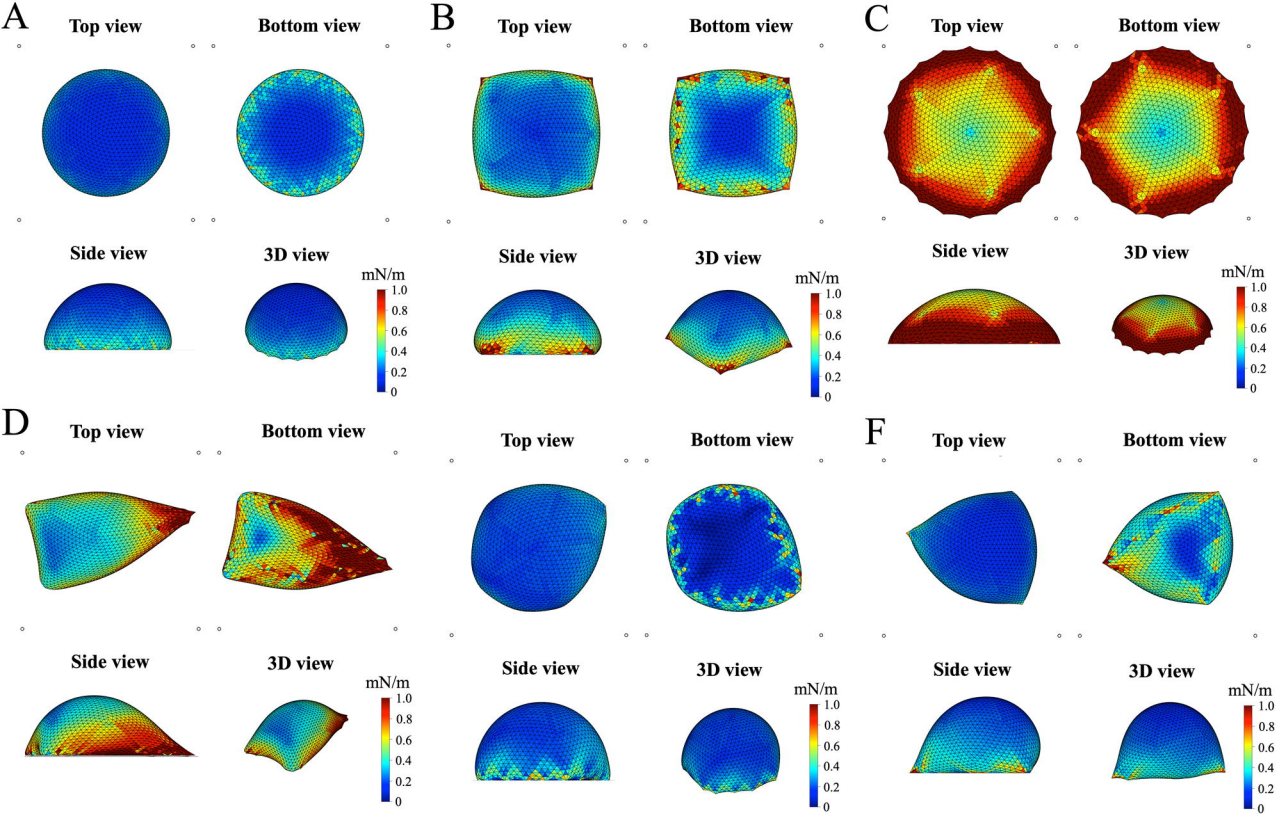
A
Top view
Bottom view
Side view
3D view
mN/m
1.0
0.8
0.6
0.4
0.2
0
B
Top view
Bottom view
Side view
3D view
mN/m
1.0
0.8
0.6
0.4
0.2
0
C
Top view
Bottom view
Side view
3D view
mN/m
1.0
0.8
0.6
0.4
0.2
0
D
Top view
Bottom view
Side view
3D view
mN/m
1.0
0.8
0.6
0.4
0.2
0
Top view
Bottom view
Side view
3D view
mN/m
1.0
0.8
0.6
0.4
0.2
0
F
Top view
Bottom view
Side view
3D view
mN/m
1.0
0.8
0.6
0.4
0.2
0

Relevances of CCPs number, geometric parameters and tension (Total 12 cells)

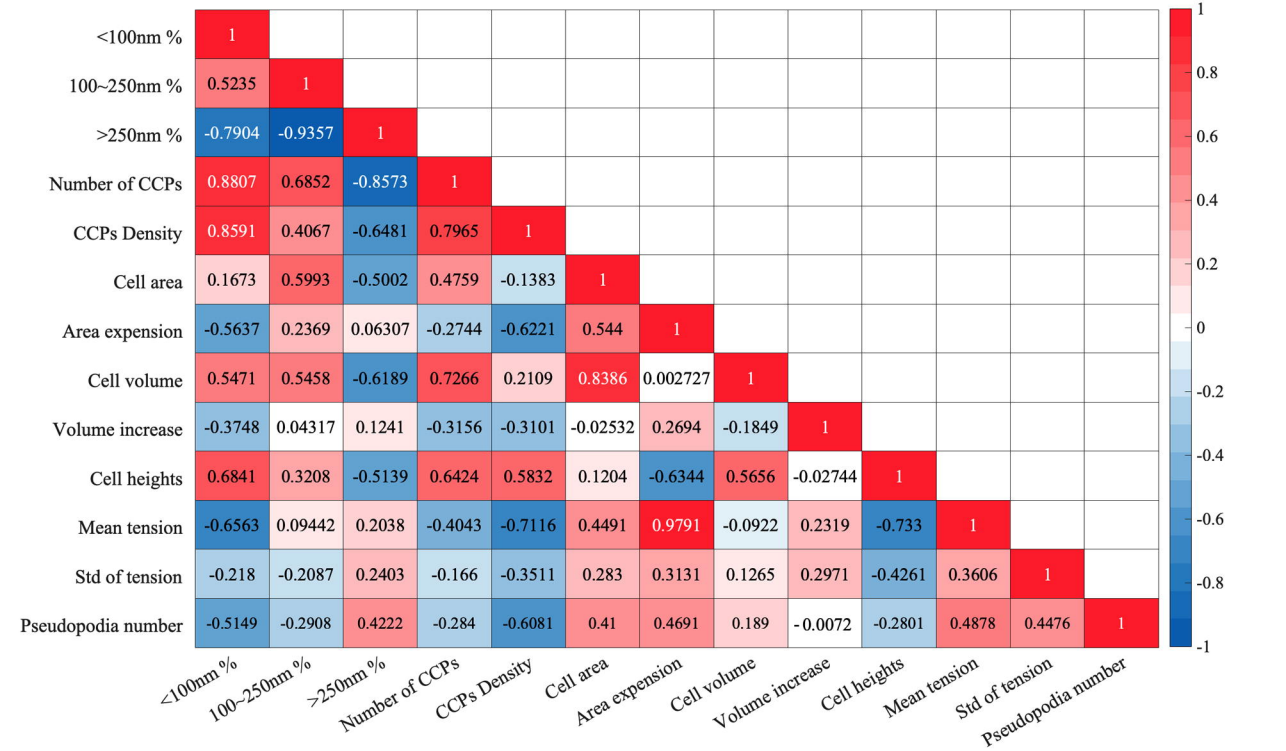

A

(1)

(2)

(3)

(4)

CCPs locations on Cell ID.11

CCPs size histogram

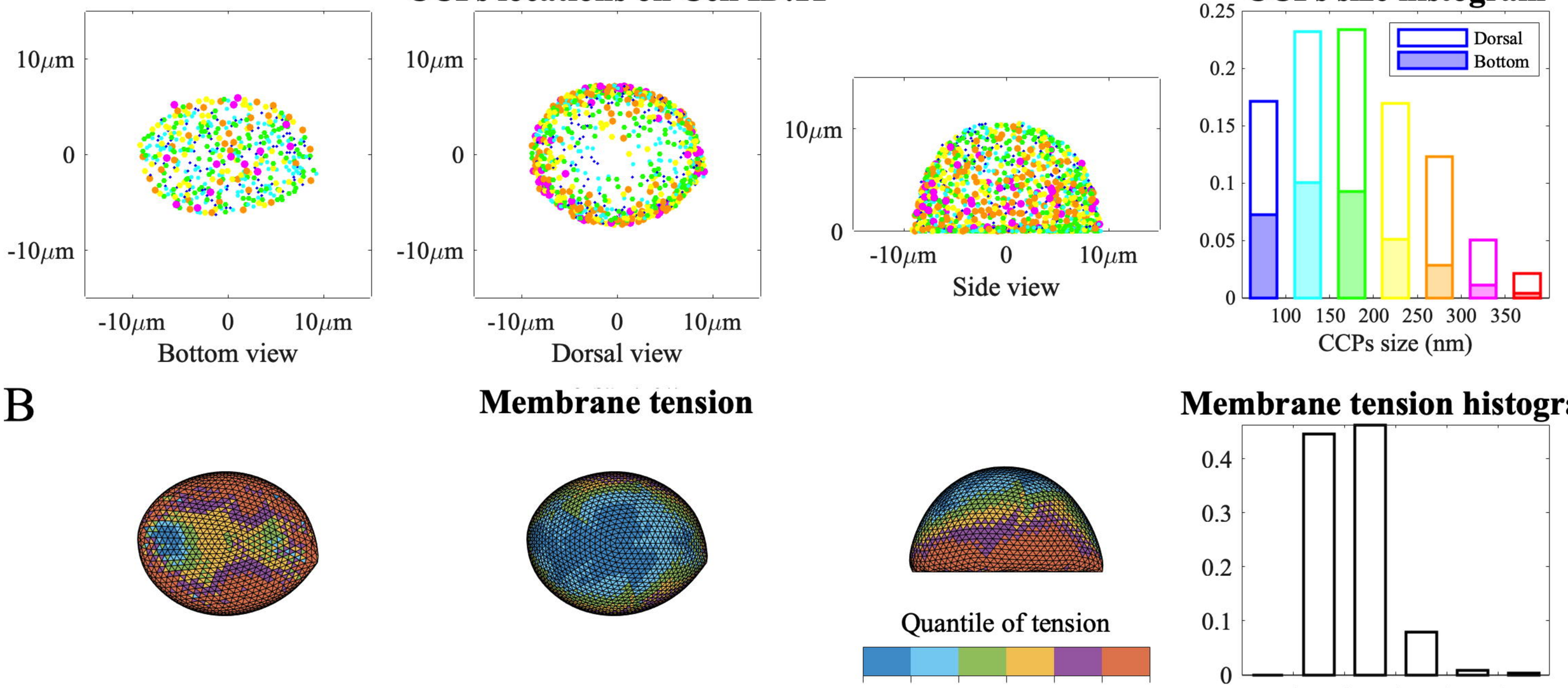

B

Membrane tension

Membrane tension histogram

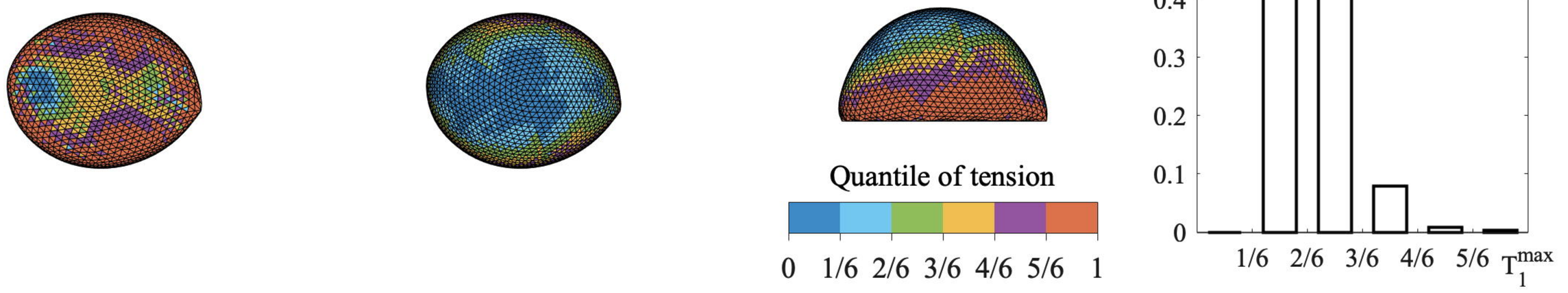

C

Background tension distribution of CCPs

CCPs numbers in six quantiles of membrane tension

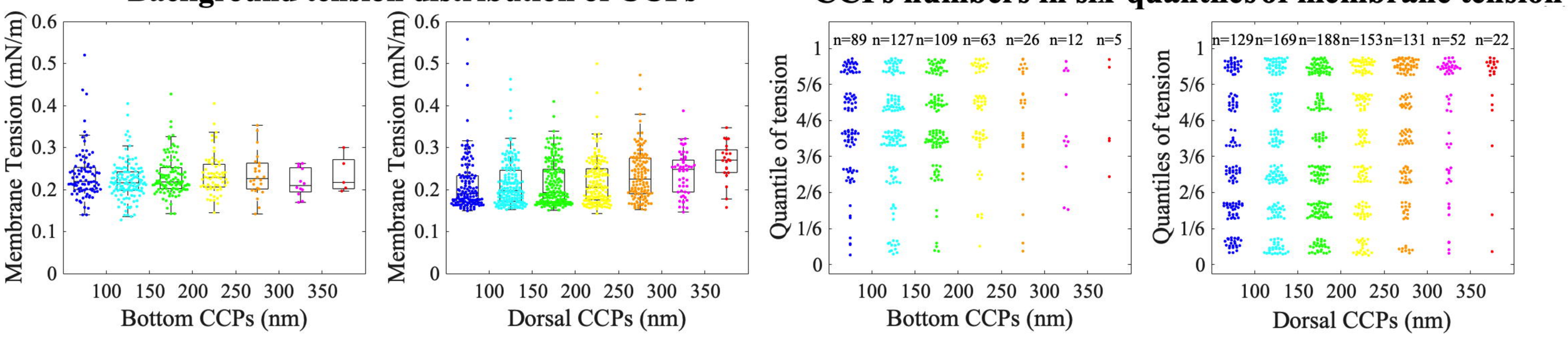

D

CCPs histogram sorted by tension quantiles

Relevance

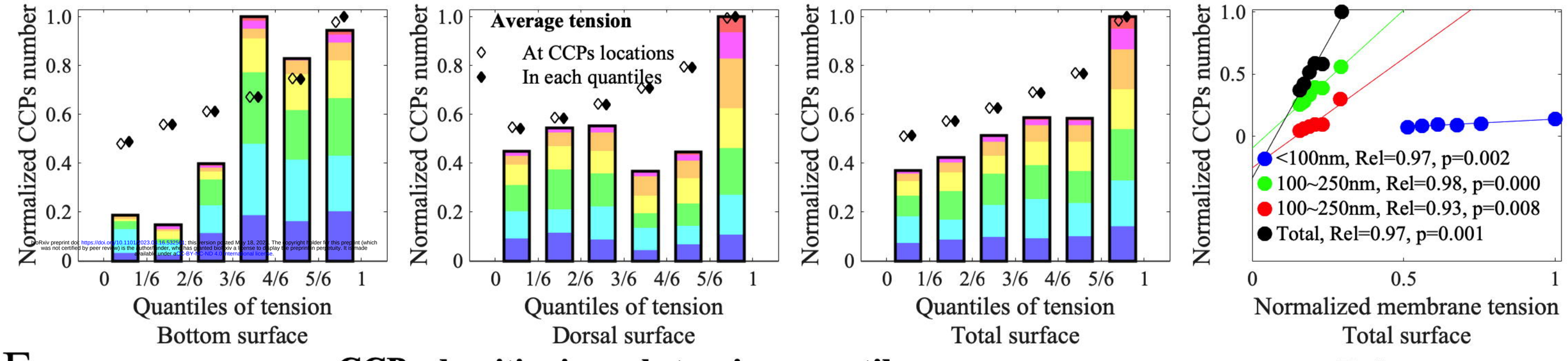

E

CCPs densities in each tension quantiles

Relevance

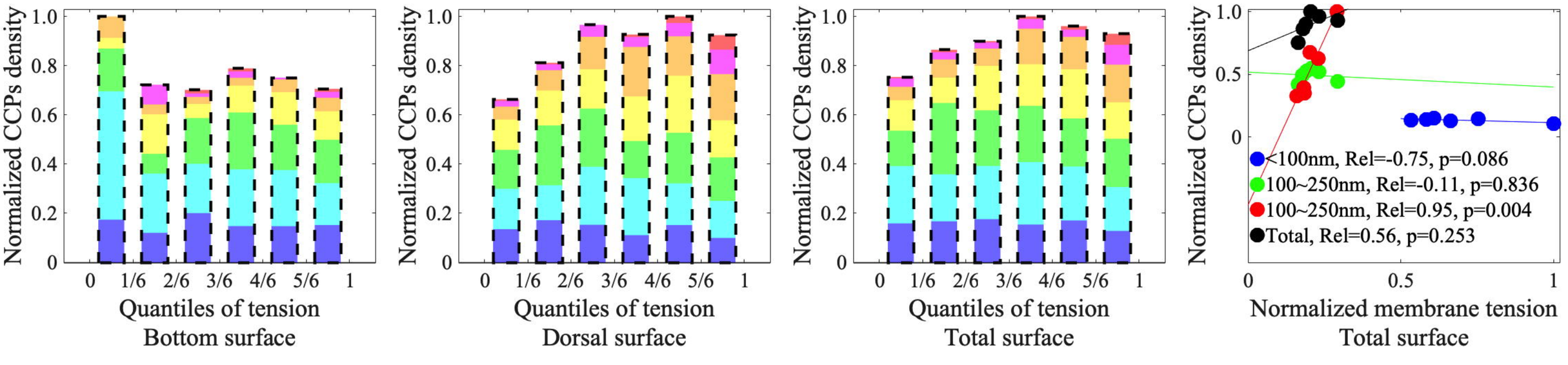

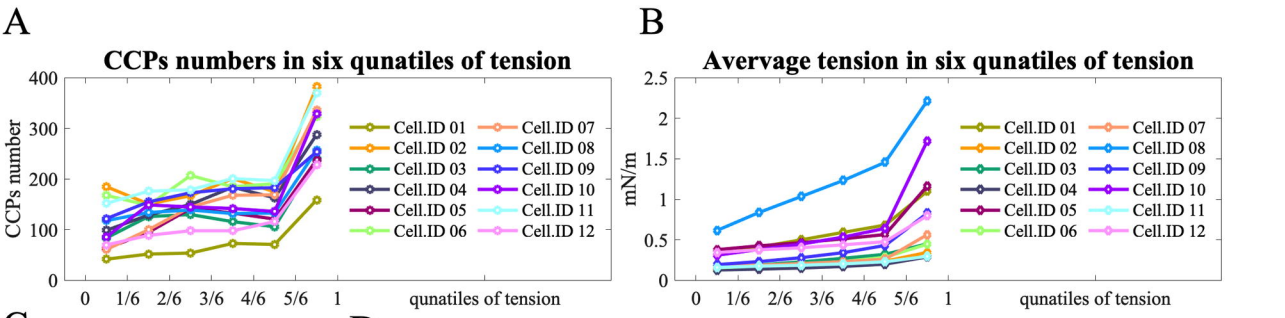

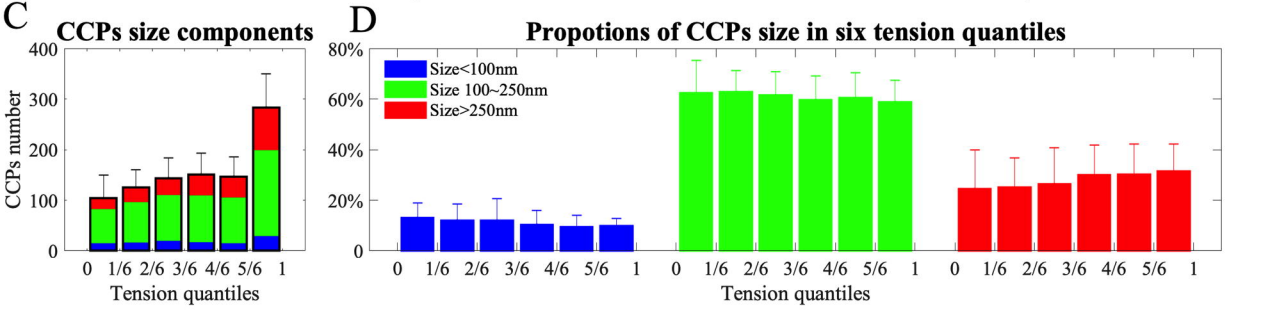

E

CCPs numbers in six quintiles vs. tension in six quantiles

	<100nm	100~250 nm	>250nm	All
Cell.ID 01	0.8338	0.9682	0.8797	0.9439
Cell.ID 02	0.6674	0.9071	0.8135	0.89
Cell.ID 03	0.3216	0.8277	0.8977	0.8439
Cell.ID 04	0.7371	0.8994	0.9475	0.9558
Cell.ID 05	0.8596	0.9293	0.8832	0.9412
Cell.ID 06	0.1672	0.964	0.9845	0.9354
Cell.ID 07	0.9467	0.9383	0.9436	0.9231
Cell.ID 08	0.7932	0.9033	0.909	0.9244
Cell.ID 09	0.612	0.822	0.9646	0.9599
Cell.ID 10	0.6139	0.9555	0.9245	0.9559
Cell.ID 11	0.9045	0.9395	0.9402	0.9451
Cell.ID 12	0.9205	0.9731	0.9947	0.9962

F

CCPs densities in six quintiles vs. tension in six quantiles

	<100nm	100~250 nm	>250nm	All
Cell.ID 01	0.4947	0.6795	0.9603	0.9042
Cell.ID 02	-0.4783	0.4312	0.7459	0.4156
Cell.ID 03	-0.3991	0.1877	0.465	0.271
Cell.ID 04	-0.5594	0.2289	0.7477	0.3221
Cell.ID 05	0.1567	0.43	0.2146	0.3612
Cell.ID 06	-0.3269	-0.3177	0.7731	-0.0617
Cell.ID 07	0.5428	0.3661	0.5871	0.4125
Cell.ID 08	0.4575	-0.9683	0.4877	-0.2234
Cell.ID 09	-0.4767	-0.2395	0.6294	-0.08717
Cell.ID 10	-0.3396	0.7288	0.1686	0.4732
Cell.ID 11	-0.7505	-0.1096	0.9492	0.5554
Cell.ID 12	0.6151	0.5816	0.6561	0.7208

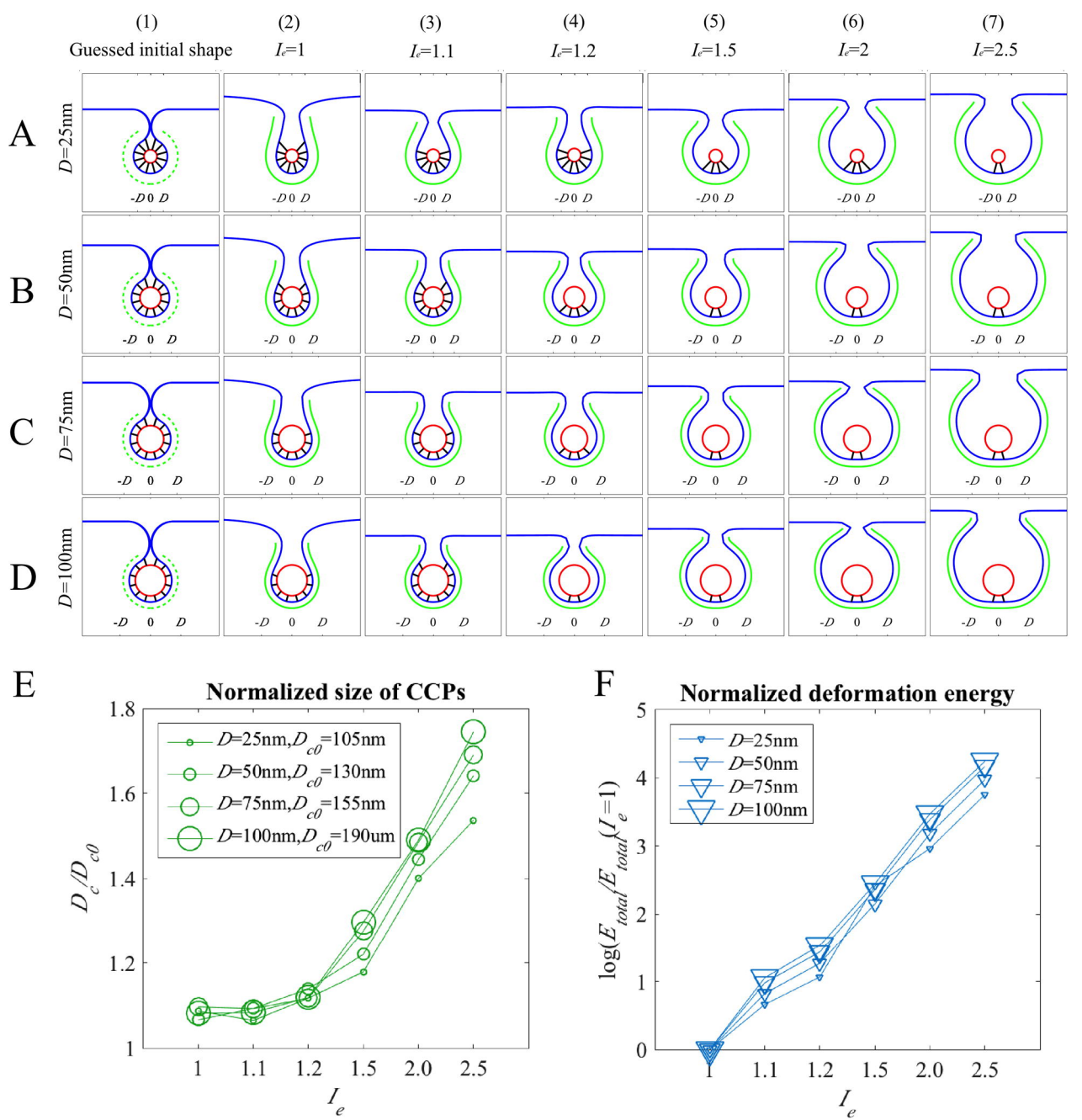
(1)
Guessed initial shape
(2)
I_e=1
(3)
I_e=1.1
(4)
I_e=1.2
(5)
I_e=1.5
(6)
I_e=2
(7)
I_e=2.5
A
B
C
D
D=25nm
D=50nm
D=75nm
D=100nm
-D 0 D
E
Normalized size of CCPs
D=25nm,D_{c0}=105nm
D=50nm,D_{c0}=130nm
D=75nm,D_{c0}=155nm
D=100nm,D_{c0}=190um
D_c/D_{c0}
I_e
F
Normalized deformation energy
D=25nm
D=50nm
D=75nm
D=100nm
$\log(E_{total}/E_{total}(I_e=1))$
I_e